

# Single Electron Charging in Optically Active Nanowire Quantum Dots

Maarten P. van Kouwen,<sup>†</sup> Michael E. Reimer,<sup>†</sup> Anne W. Hidma,<sup>†</sup> Maarten H. M. van Weert,<sup>†</sup> Rienk E. Algra,<sup>†,||</sup> Erik P. A. M. Bakkers,<sup>†,†,§</sup> Leo P. Kouwenhoven,<sup>\*,†</sup> and Val Zwiller<sup>†</sup>

<sup>†</sup>Kavli Institute of Nanoscience, Delft, The Netherlands, <sup>†</sup>Philips Research Laboratories, Eindhoven, The Netherlands, and <sup>§</sup>Eindhoven University of Technology, The Netherlands

**ABSTRACT** We report optical experiments of a charge tunable, single nanowire quantum dot subject to an electric field tuned by two independent voltages. First, we control tunneling events through an applied electric field along the nanowire growth direction. Second, we modify the chemical potential in the nanowire with a back-gate. We combine these two field-effects to isolate a single electron and independently tune the tunnel coupling of the quantum dot with the contacts. Such charge control is a first requirement for opto-electrical single electron spin experiments on a nanowire quantum dot.

**KEYWORDS** Nanowires, optically-active quantum dots, single electron charging, opto-electronics

Single, optically active quantum dots are widely investigated due to the ability to combine both single electron charging<sup>1,2</sup> and single<sup>3</sup> or entangled<sup>4</sup> photon-emission, which are all key requirements for quantum information processing applications.<sup>5</sup> Nanowire quantum dots (NW-QDs) offer additional functionalities over self-assembled quantum dots since they are embedded in a one-dimensional system instead of a three-dimensional host matrix. Therefore, the single electron (hole) transport channel is naturally aligned to the optically active quantum dot in the nanowire, advantageous for combining both quantum optics<sup>6</sup> and transport.<sup>7–9</sup> In addition, due to the small radial dimensions of the nanowires, electrostatic gate geometries are highly versatile<sup>7,8</sup> and axial heterostructure design is not limited by strain. As an example, the combination of Si sections, which are free of nuclear spins, with optically addressable electronic levels in III–V materials is promising for extending electron spin storage times. Prior to the work presented here, we have shown that a single InAsP quantum dot grown in an InP nanowire geometry is optically active, exhibits narrow emission lines, spin polarization memory effects,<sup>10</sup> and can be embedded in a LED device geometry.<sup>11</sup> Furthermore, it is predicted that NW-QDs are ideal sources of entangled photons due to the nanowire symmetry.<sup>12</sup> Recently, an electron spin-to-charge conversion read-out scheme has been proposed,<sup>13</sup> which is compatible with controlled storage of carriers up to microseconds.<sup>14</sup> Such storage times are promising since single spins in self-assembled quantum dots (SA-QDs) have been initialized,

coherently manipulated, and read-out within picosecond time scales.<sup>15,16</sup> The proposed spin read-out scheme<sup>13</sup> highly depends on the overall tunnel coupling between the SA-QD energy levels and the continuum, determined by the quantum dot-to-contact spatial separation, which is fixed during growth.<sup>17</sup>

In this letter, we present electrical control and optical read-out of the number of electrons residing in a single InAs<sub>0.25</sub>P<sub>0.75</sub> quantum dot embedded in an InP nanowire. We first identify the neutral exciton by photocurrent spectroscopy. Second, we demonstrate that the electron number can be controlled by an electric field applied along the nanowire growth direction or by an electrostatic back-gate that modifies the overall potential landscape of the nanowire. Finally, we tune the tunnel coupling of the quantum dot to the leads independently of the charge state.

Our nanowires have a typical length of 4  $\mu\text{m}$  and a tapered diameter of 20 nm at the apex versus 60 nm at the base (Figure 1a). The nanowires have no intentional doping. The InAs<sub>0.25</sub>P<sub>0.75</sub> quantum dot is between 4–6 nm high and  $\sim 30$  nm in diameter.<sup>10</sup> The nanowires are contacted by a titanium (Ti) source and drain, while the p<sup>++</sup>-Si/SiO<sub>2</sub> substrate forms a back-gate (Methods). Figure 1b presents the device geometry and circuit schematics. At the Ti-InP interface, the Fermi level is pinned  $\sim 200$  meV below the InP conduction band.<sup>18</sup> Therefore, Schottky barriers are formed and a source-drain voltage  $V_{\text{sd}}$  generates an electric field along the nanowire growth axis without inducing a high current ( $I < 8$  pA at  $V_{\text{sd}} < 6$  V). In addition, the charge density in the nanowire can be changed with the back-gate voltage  $V_{\text{g}}$ .

Figure 1c presents the photoluminescence from a single NW-QD as a function of incident laser power under non-resonant continuous wave excitation and at  $V_{\text{sd}} = V_{\text{g}} = 0$  V. Here, the quantum dot is expected to be negatively charged

\* To whom correspondence should be addressed. E-mail: l.p.kouwenhoven@tudelft.nl.

|| Author is also at Materials Innovation Institute (M2I), Delft 2628CD, The Netherlands and IMM, Solid State Chemistry, Radboud University Nijmegen, Nijmegen 6525AJ, The Netherlands.

Received for review: 02/11/2010

Published on Web: 04/13/2010

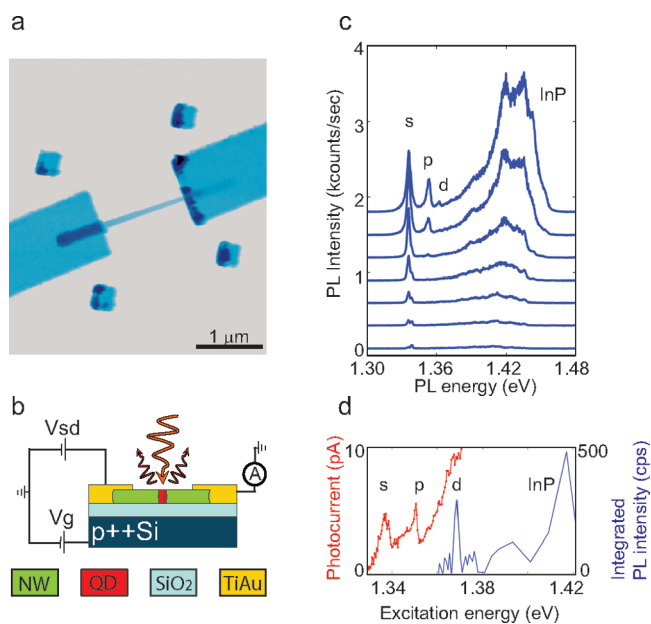


**FIGURE 1.** (a) Typical atomic force microscopy image of a contacted nanowire containing a single quantum dot. (b) Schematic cross-section of the contacted nanowire (NW) quantum dot (QD) on a substrate containing a back-gate. (c) Photoluminescence spectra under increasing excitation intensity. (Excitation energy = 2.33 eV, source-drain bias,  $V_{sd}$  = 0 V, back gate potential,  $V_g$  = 0 V, integration time,  $dt$  = 1 s). (d) The NW InP and QD s-p and d-shell resonances. Blue line: photoluminescence of the s-shell as a function of laser excitation energy (PLE). Red line: photocurrent as a function of laser excitation energy (PCE). (PLE: laser intensity = 10 W/cm<sup>2</sup>,  $V_{sd}$  = 5.4 V,  $V_g$  = -9 V,  $dt$  = 10 s. PCE: laser intensity = 100 W/cm<sup>2</sup>,  $V_{sd}$  = 6 V,  $V_g$  = -9 V).

due to the Fermi level pinning at the nanowire surface.<sup>18</sup> (The exact determination of the number of excess charges residing in the quantum dot is determined below using resonant photocurrent experiments). In photoluminescence at low excitation power, a single peak is observed at 1.335 eV attributed to the recombination of a single electron-hole pair in the quantum dot s-shell. At higher excitation power, the s-shell emission consists of an excitonic and biexcitonic peak, described in more detail in reference.<sup>10</sup> With increasing excitation power, a second (p, 1.352 eV) and third (d, 1.361 eV) shell appear as the lower energy transitions in the NW-QD become saturated. The broad emission peak observed around 1.42 eV is due to InP carrier recombination.<sup>19</sup> Figure 1d presents a photoluminescence excitation (PLE) spectrum (blue line), obtained by integrating the s-shell photoemission intensity at varying laser excitation energies. In the PLE spectrum, the InP and d-shell absorption resonances are detected using the s-shell emission. Laser filter constraints inhibit PLE measurements below 1.36 eV excitation energy. Therefore, resonant photocurrent spectroscopy (Figure 1d, red line) is performed to demonstrate resonant absorption in the s-, p-, and d-shells. Here, the photoexcited electron-hole (e-h) pairs are separated by an applied bias of  $V_{sd}$  = 6 V. The energy difference between the s- and p-shell resonances (the s-p orbital splitting) is determined by the quantum dot radial confinement. The splitting is found to

be 17 meV and is similar to InAs/InP SA-QDs of comparable size.<sup>20</sup> To avoid screening of applied electric fields due to photoexcited carriers in the InP barrier region, photoluminescence experiments are performed under quantum dot d-shell quasi resonant excitation (1.361 eV) in the remainder of this letter. The s-shell photocurrent resonance at  $V_{sd}$  = 6 V is found at 1.3394 eV excitation energy while the emission energy at  $V_{sd}$  = 0 V is found at 1.335 eV in Figure 1c.

In Figure 2a (top), photoluminescence from the quantum dot s-shell is presented as a function of  $V_{sd}$  in the bias range between 0 and 6 V. The corresponding integrated photoluminescence intensity is shown in Figure 2a (bottom). In addition, Figure 2a (bottom) compares the source-drain current in absence of illumination (black line) to the s-shell resonant photocurrent (red line), which is excited at the 1.3394 eV resonance presented in Figure 1d. Above  $V_{sd}$  = 3.8 V, no photoluminescence is observed. In photocurrent spectroscopy, however, a resonance peak of ~8 pA is measured. In this bias regime, the applied electric field compensates for the Coulomb attraction of the electron-hole pair and in addition reduces the tunnel barriers. Therefore, the photoexcited carriers tunnel out of the quantum dot before undergoing radiative recombination. When reducing the bias to 3.5 V, a single emission peak emerges at the same energy of 1.3394 eV (line width 280 μeV). The increase in photoemission coincides with a decrease in the resonant photocurrent, displaying the competition between photoemission (at rate  $\Gamma_{rad}$ ) and carrier tunneling (at rate  $\Gamma_{escape}$ ) from the same optical transition. The corresponding transitions are presented in Figure 2b (top). On the basis of the presented resonant photocurrent measurements, the optical transition at 1.3394 eV is identified as the neutral exciton  $X^0$  involving single electron-hole pair recombination in the quantum dot s-shell.

The onset voltage for the  $X^0$  resonant photocurrent is independent of the excitation intensity since the single exciton escape rate,  $\Gamma_{escape}$ , is determined by the applied electric field across the nanowire (see one dimensional (1D) WKB model and photocurrent laser power dependence in Supporting Information). The photocurrent reduces slightly at a bias above  $V_{sd}$  = 4 V, as the  $X^0$  resonance shifts due to the quantum confined Stark effect, which will be presented later in Figure 4d.

At approximately  $V_{sd}$  = 1.5 V, the  $X^0$  emission quenches while a new peak appears at 1.3376 eV originating from exciton recombination in the presence of an electrostatically induced electron ( $X^{1-}$ ). For the  $X^{1-}$  transition, no photocurrent resonance is observed. See Figure 2b (bottom) for an overview of the  $X^0$  and  $X^{1-}$  radiative and tunneling transitions at  $V_{sd}$  = 1.5 V. The photoluminescence transition between  $X^{1-}$  and  $X^0$  is governed by tunneling of the single electron ( $e^-$ ) in the  $X^{1-}$  final state, in which Coulomb interactions can be neglected (see WKB model in supporting material). The observed emission energy difference between  $X^{1-}$  and  $X^0$  (the  $X^{1-}$  renormalization energy) is 2 meV for

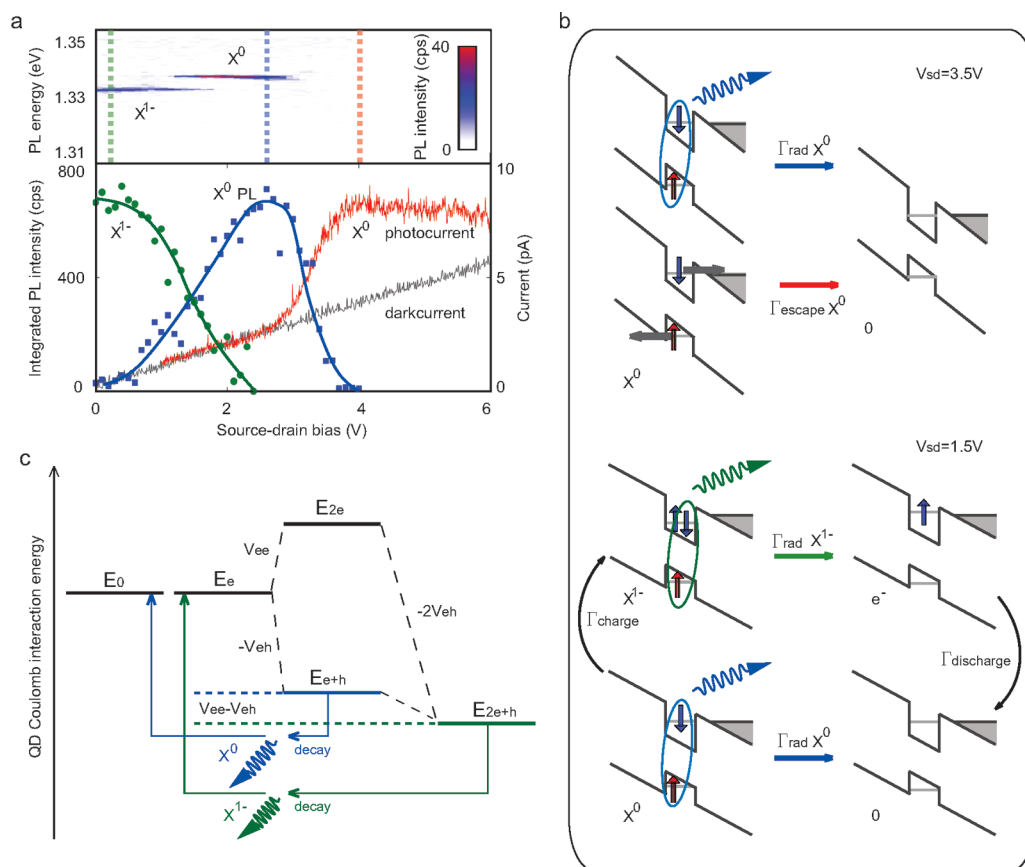


**FIGURE 2.** From light emission to photocurrent. (a) (Top) Contour plot of quasi-resonantly excited photoluminescence as a function of source-drain bias (laser intensity = 10 W/cm<sup>2</sup>, excitation energy = 1.361 eV,  $V_g = +54$  V,  $dt = 10$  s). (Bottom) Integrated photoluminescence intensity of  $X^{1-}$  (green circles with solid line as guide to the eye) and  $X^0$  (blue squares) compared to  $X^0$  resonant photocurrent (red line, laser intensity = 100 W/cm<sup>2</sup>, excitation energy = 1.3394 eV) and dark current (black line) as a function of source-drain bias. PL intensity corresponds to top, in which the maxima are indicated by dotted lines. (b) Band energy diagrams representing possible  $X^{1-}$  and  $X^0$  transitions at  $V_{sd} = 3.5$  V and  $V_{sd} = 1.5$  V. Colored horizontal arrows indicate charge neutral optical transitions and tunneling events. Colors correspond to the bottom figure in (a). Black arrows indicate (dis)charging events. (c) Effect of Coulomb interaction energies on the quantum dot conduction band energy level when adding electrons, e and holes, h. For clarity, the valence band energy is assumed to be constant.  $V_{eh}$ , e-h Coulomb attraction energy;  $V_{ee}$ , e-e repulsion;  $E_0$ , empty QD;  $E_e$ , 1 electron;  $E_h$ , 1 hole;  $E_{2e}$ , 2 electrons;  $E_{2e+h}$ , 2 electrons and 1 hole on the QD.

our NW-QD, which is similar to calculations for SA-QDs of comparable dot diameter.<sup>21</sup> Figure 2c presents the electron–hole Coulomb attraction energy  $V_{eh}$  and the electron–electron Coulomb repulsion energy  $V_{ee}$  inducing a  $X^0 - X^{1-}$  energy difference of  $V_{ee} - V_{eh}$ . The observed  $X^{1-}$  emission at lower energy implies that  $V_{eh}$  (calculated to be 40–60 meV in InAs/InP NW-QDs<sup>22</sup>) exceeds  $V_{ee}$ .

These Coulomb interactions affect the photoemission coexistence of  $X^0$  and  $X^{1-}$  (from  $V_{sd} = 0.5$  to 2 V) in Figure 2a via tunnel events in the photoexcited state. From Figure 2b (bottom) the mechanism for the  $X^0$  and  $X^{1-}$  overlap can be understood. Two tunnel events are of importance: first, when the source-drain bias is increased, the tunnel probability ( $\Gamma_{discharge}$ ) of the  $X^{1-}$  final state electron ( $e^-$ ) through the triangular shaped tunnel barrier increases; second, the quantum dot can recharge via initial state tunneling ( $\Gamma_{charge}$ ). The second charging event is driven by the quantum dot energy, which is higher in the  $X^0$  initial state than in the initial state of  $X^{1-}$  due to Coulomb interactions (see Figure 2c). A low tunneling probability ( $\Gamma_{charge} \sim \Gamma_{rad}$ ) can allow for  $X^0$

recombination before an energetically favorable electron tunnels into the quantum dot to result in  $X^{1-}$  emission. In contrast, when the tunnel coupling is high ( $\Gamma_{charge} > \Gamma_{rad}$ ), the quantum dot charge state can easily change to follow the chemical potential. Hence, at high tunnel coupling the  $X^0 - X^{1-}$  transition is expected to be more abrupt.<sup>17</sup>

Instead of controlling the electron number in our NW-QD by electric field induced tunnel events along the nanowire growth direction (source-drain bias), the back-gate potential can be utilized to tune the Fermi level in the nanowire with respect to the energy levels in the quantum dot. In Figure 3a, high-resolution photoluminescence spectra are presented as a function of back-gate voltage ( $V_{sd} = 0$  V). At large negative back-gate bias ( $V_g = -42$  V),  $X^0$  is observed at 1.3394 eV. At  $\sim V_g = -35$  V,  $X^{1-}$  recombination appears in the optical spectrum while  $X^0$  quenches. Here, the Fermi-level in the nanowire is aligned with the quantum dot electron s-shell. Reducing the large negative back-gate bias further results in an unstable regime of the optical spectra between  $-20$  V and  $+5$  V, indicating that the quantum dot

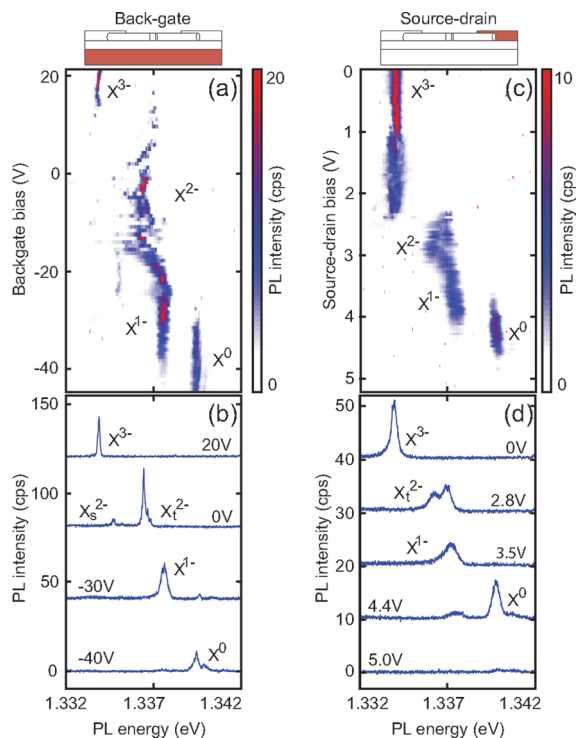


**FIGURE 3.** High-resolution s-shell photoluminescence as a function of back-gate ( $V_g$ ) and source-drain ( $V_{sd}$ ) bias. (a) Contour plot of the photoluminescence at varying back-gate voltages. Corresponding linetraces presented in (b). (Top) Back-gate is depicted in red (laser intensity =  $10 \text{ W/cm}^2$ , excitation energy =  $1.361 \text{ eV}$ ,  $V_{sd} = 0 \text{ V}$ ,  $dt = 80 \text{ s}$ ). (c) Contour plot of the photoluminescence at varying source-drain bias voltages. Corresponding line traces presented in (d). (Top) Source contact is depicted in red (laser intensity =  $10 \text{ W/cm}^2$ , excitation energy =  $1.361 \text{ eV}$ ,  $V_g = +54 \text{ V}$ ,  $dt = 80 \text{ s}$ ).

suffers from charge fluctuations in its environment.<sup>25</sup> Even though the optical spectra are unstable over long time-scales, line traces in Figure 3b show that the emission at  $V_g = 0 \text{ V}$  consists of two peaks. The intensity of the lower energy peak is 1 order of magnitude smaller than the higher energy peak. We attribute the two observed peaks at  $V_g = 0 \text{ V}$  to  $X_s^{2-}$  since  $X_t^{2-}$  recombination typically consists of a singlet ( $X_s^{2-}$ ) and a triplet ( $X_t^{2-}$ ) emission line, which are separated by twice the s-p exchange interaction.<sup>24</sup> The observed intensity of  $X_s^{2-}$  is expected to be lower than  $X_t^{2-}$  due to the number of possible final states.<sup>24</sup> At  $V_{sd} = V_g = 0 \text{ V}$ , the quantum dot is charged with 2 extra electrons caused by the Fermi level pinning at the nanowire surface.<sup>18</sup> At large positive back-gate voltages ( $V_g > 15 \text{ V}$ ), the emission stabilizes and a peak (line width of  $160 \mu\text{eV}$ ) at  $1.3339 \text{ eV}$  is observed. We assign this line to  $X^3$  involving s-shell exciton recombination in the presence of three additional electrons. Note that the observed emission line width is larger than expected from the exciton lifetime. Presumably the dynamics of the nanowire surface states cause inhomogeneous broadening of the emission lines.

In Figure 3c, high-resolution photoluminescence spectra are presented as a function of source-drain bias at a fixed back-gate voltage of  $V_g = +54 \text{ V}$ . At  $V_{sd} = 0 \text{ V}$ ,  $X^{3-}$  emission

is observed. When increasing the electric field along the nanowire elongation axis, the quantum dot discharges. Here,  $X^{3-}$ ,  $X_t^{2-}$ ,  $X^{1-}$ , and  $X^0$  emission are observed successively before quenching of the quantum dot photoluminescence at  $V_{sd} = 4.7 \text{ V}$ . It should be noted that  $X_s^{2-}$  emission is not observed here due to the lower intensity obtained for the source-drain sweep compared to the back-gate voltage sweep.

The back-gate and source-drain bias can now be combined to tune the charge density in the nanowire and control the quantum dot tunnel events. In Figure 4a–c, the quantum dot photoluminescence is plotted as a function of  $V_{sd}$  for corresponding  $V_g = -18, 0, \text{ and } +18 \text{ V}$ . Extracted from Figures 4a–c, we first study the effect of the back-gate bias on the observed  $X^0$  quantum confined Stark effect (QCSE) in Figure 4d. When assuming a homogeneous electric field,  $F = V_{sd}/l$  (with  $l = 1.4 \mu\text{m}$ , the electrode spacing), the QCSE shifts are determined to be  $-1.5, -1.2, \text{ and } -1.7 \mu\text{eV/cm}^2\text{kV}^2$  for  $V_g = -18, 0, \text{ and } +18 \text{ V}$ , respectively. These values are comparable to Stark shifts obtained in self-assembled InAs-InP quantum dots of similar quantum dot height.<sup>25</sup> A more significant effect of the back-gate potential on the quantum dot emission is the observed coexistence variation of  $X^{1-}$  and  $X^0$  in Figures 4a–c. Here, the NW-QD is tuned from a regime in which  $X^0$  and  $X^{1-}$  are highly overlapping (for a range of  $\sim 2 \text{ V}$  in Figure 4a) to a regime in which the peaks are virtually nonoverlapping (Figure 4c) indicating that the tunnel coupling (i.e.,  $\Gamma_{\text{charge}}$  and  $\Gamma_{\text{discharge}}$ ) from the quantum dot to the contacts is strongly modified. The graphic representation of the  $X^0$  and  $X^{1-}$  emission in Figure 4e explicitly demonstrates that the coexistence is reduced with increasing back-gate bias voltage. The altered nanowire carrier-density by the back-gate changes the charge state of the quantum dot (Figure 3b) and in addition affects the transparency of the Schottky barriers, thus modifying the tunnel coupling. The reduced escape voltage of  $X^0$  confirms the tunnel coupling enhancement. At this high tunnel coupling, we could estimate an electron charging energy of  $8 \text{ meV}$ , extracted from the length of the charge plateaus of  $X^{1-}$  ( $1.75 \text{ V}$ ) and  $X^0$  ( $0.7 \text{ V}$ ) in a similar manner to the work of Seidl and co-workers.<sup>26</sup> In contrast to that work, we also utilize the conduction band s-p orbital energy splitting ( $11.3 \text{ meV}$ ) to estimate a coupling strength ( $0.011$ ) of the contacts to the quantum dot, which provides a relationship between the applied voltage and the electron charging energy. The s-p orbital energy splitting is estimated by assuming a 2:1 electron versus hole orbital energy ratio, which is determined for InAs/InP quantum dots.<sup>27</sup> The total s-p orbital splitting of  $17 \text{ meV}$  was obtained from Figure 1c.

The tunability of the tunnel coupling in an optically active quantum dot enables the optimization of tunnel rates with respect to the exciton radiative lifetime, which is crucial for any electron spin-to-charge optical read-out scheme.

In conclusion, we have presented single electron charging in an optically active nanowire quantum dot. We showed by photoluminescence spectroscopy that the exciton charge

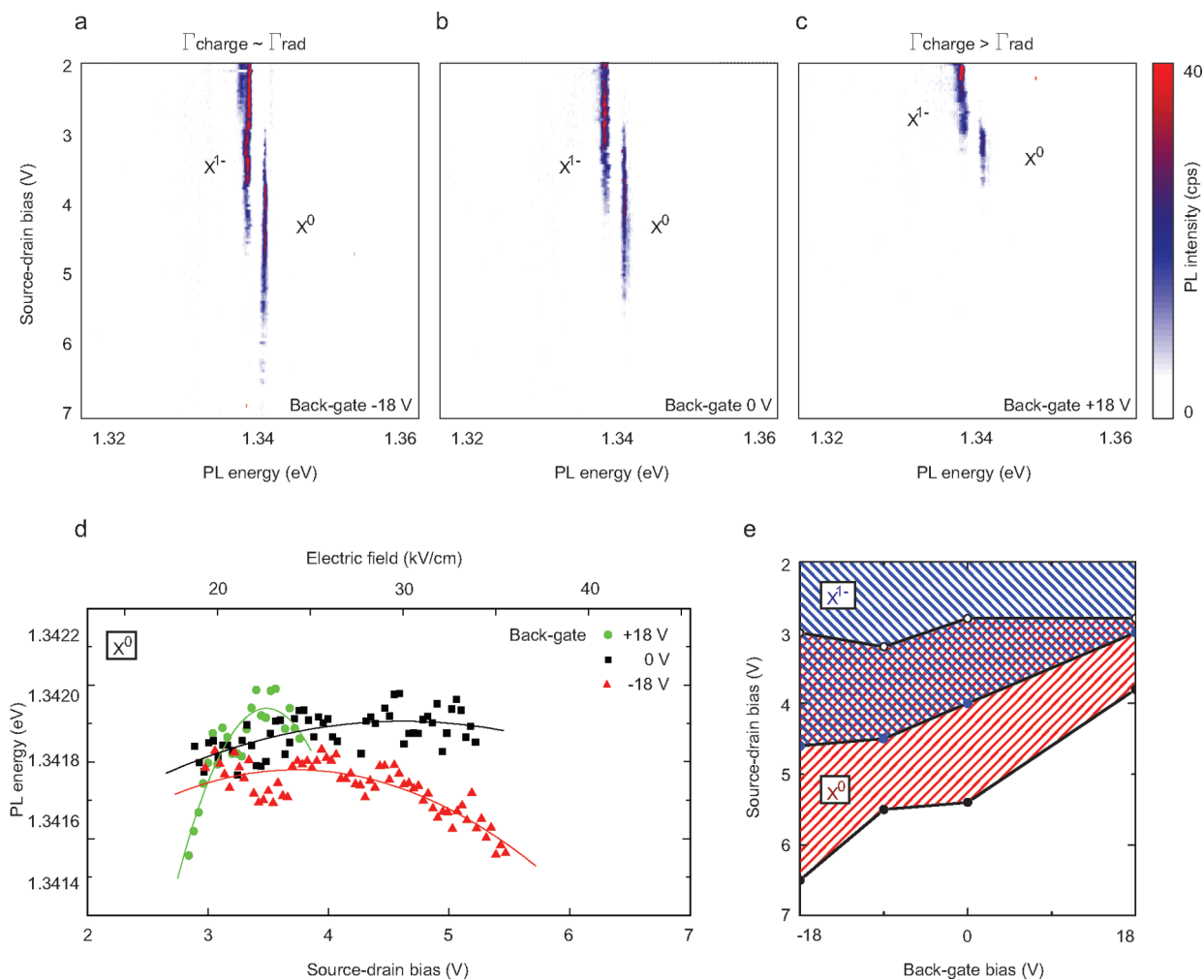


FIGURE 4. Effect of the back-gate potential on the exciton emission energy and tunnel coupling. (a–c) Photoluminescence as a function of source-drain bias presenting  $X^0$  and  $X^{1-}$  emission at three different back gate potentials (laser intensity =  $10 \text{ W/cm}^2$ , excitation energy =  $1.361 \text{ eV}$ ,  $V_g = -18, 0$ , and  $+18 \text{ V}$ ,  $dt = 5 \text{ s}$ ). (d)  $X^0$  recombination energy as function of source-drain bias at  $V_g = -18 \text{ V}$  (red triangles),  $V_g = 0 \text{ V}$  (black squares), and  $V_g = +18 \text{ V}$  (green circles), extracted from panels (a), (b), and (c). Lines correspond to a second order polynomial fit. Electric field is assumed to be homogeneous along the nanowire elongation axis. (e) Range of  $X^{1-}$  and  $X^0$  emission and coexistence as a function of source-drain and back-gate bias.

state was tuned by two independent mechanisms, electric field-induced tunneling along the nanowire growth axis and chemical potential tuning with a back-gate. We combined these two mechanisms to isolate a single electron within the optically active quantum dot and tune the quantum dot tunnel coupling with the contacts. The device geometry allows for addition of multiple lateral electrostatic gates to a single quantum dot. These results demonstrate that nanowire devices are promising for future single electron (spin) opto-electrical experiments such as coherent electrical spin manipulation followed by optical read-out and conversion of electron spin into photon polarization for long distance transfer of quantum information.

#### Methods. Nanowire Growth and Device Fabrication.

The nanowire quantum dots were grown in the vapor–liquid–solid mode<sup>28</sup> by means of metal–organic vapor-phase epitaxy in a similar manner as reported by Minot et al.<sup>11</sup> Colloidal Au particles of  $20 \text{ nm}$  diameter were used to

first grow an InP section for  $20 \text{ min}$  ( $\sim 2 \mu\text{m}$ ) followed by  $1 \text{ s}$  of InAsP growth. The  $\sim 4 \mu\text{m}$  long nanowires were completed by another  $20 \text{ min}$  of InP growth. By energy dispersive X-ray analysis in a transmission electron microscope, the dot size for  $2 \text{ s}$  of growth was estimated to be  $9 \pm 1 \text{ nm}$  high and  $33 \pm 1 \text{ nm}$  in diameter.<sup>10</sup> After growth, the InP nanowires were transferred from the InP growth substrate to a prepatterned  $p^{++}$  silicon wafer with thermal oxide layer of  $290 \text{ nm}$ . Characterization by microphotoluminescence ( $\mu\text{PL}$ , see below) was done to select individual quantum dots with emission linewidths below  $400 \mu\text{eV}$ . Nanowire identification and electrode positioning were done with the use of markers by optical microscope imaging. Electrode patterning was done by e-beam lithography. Before metal deposition, HF ( $6 \text{ s}$  in  $6:1$  buffered HF) was used to remove the InP native oxide layer. The contacts consist of an evaporated titanium ( $110 \text{ nm}$ )/gold ( $10 \text{ nm}$ )

thin film. Out of 35 selected nanowires, 20 single nanowire quantum dots were successfully contacted.

**Experimental Setup.**  $\mu$ PL studies were performed at 4.2 K (Figures 1c, 3, and 4) and 10 K (Figure 2). The cryostat is mounted with electrical access and a computer controlled motorized stage. Optical excitation was performed with a diode laser (photon energy 2.33 eV) and a tunable titanium sapphire laser (photon tuning energy range of 1.24–1.77 eV). A 0.65 NA objective was used. The incident linear laser polarization was modified by a half-wave plate to align the linear polarization along the nanowire elongation axis to maximize the excitation efficiency. Detection of the emitted photons was achieved through a single grating spectrometer with a nitrogen-cooled CCD. The collection efficiency of the setup was  $\sim 2\%$ . Biases were applied using battery driven voltage sources, controlled by computer via an optical fiber enabling currents as low as 10 fA to be measured.

**Acknowledgment.** We acknowledge U. Perinetti and N. Akopian for setup development, Y. Beyer, M. den Heijer, A. Weldelessi, G. Steele, J. van Tilburg, X. Liu, and Y.-M. Niquet for help and fruitful discussions, and R. N. Schouten and W. G. G. Immink for technical assistance. This work was supported by the Dutch ministry of economic affairs (NanoNed DOE7013), the Dutch Organization for Fundamental Research on Matter (FOM), the European FP6 NODE (015783) project, the DARPA QuEST grant HR0011-09-1-0007 and The Netherlands Organization for Scientific Research (NWO). The work of REA was carried out under project number MC3.0524 in the framework of the strategic research program of the Materials Innovation Institute (M2I) ([www.m2i.nl](http://www.m2i.nl)).

**Note Added after ASAP Publication.** There were minor text corrections in the version of this paper published ASAP April 13, 2010; the corrected version published ASAP April 19, 2010.

**Supporting Information Available.** One dimensional WKB tunneling model and resonant photocurrent as a function of laser intensity. This material is available free of charge via the Internet at <http://pubs.acs.org>.

## REFERENCES AND NOTES

- Hartmann, A.; Ducommun, Y.; Kapon, E.; Hohenester, U.; Molinari, E. *Phys. Rev. Lett.* **2000**, *84*, 5648.
- Findeis, F.; Baier, M.; Zrenner, A.; Bichler, M.; Abstreiter, G.; Hohenester, U.; Molinari, E. *Phys. Rev. B* **2000**, *63*, 121309-R.
- Michler, P.; Kiraz, A.; Becher, C.; Schoenfeld, W. V.; Petroff, P. M.; Zhang, L.; Hu, E.; Imamoglu, A. *Science* **2000**, *290*, 2282.
- Akopian, N.; Lindner, N. H.; Poem, E.; Berlatzky, Y.; Avron, J.; Gershoni, D.; Gerardot, B. D.; Petroff, P. M. *Phys. Rev. Lett.* **2006**, *96*, 130501.
- Gisin, N.; Thew, R. *Nat. Photonics* **2007**, *1*, 165.
- Borgström, M. T.; Zwiller, V.; Muller, E.; Imamoglu, A. *Nano Lett.* **2005**, *5*, 1439.
- Pfund, A.; Shorubalko, I.; Leturcq, R.; Ensslin, K. *Appl. Phys. Lett.* **2006**, *89*, 252106.
- Fuhrer, A.; Froberg, L.; Pedersen, J.; Larsson, M.; Wacker, A.; Pistol, M. E.; Samuelson, L. *Nano Lett.* **2007**, *7*, 243.
- De Franceschi, S.; van Dam, J.; Bakkers, E.; Feiner, L. F.; Gurevich, L.; Kouwenhoven, L. *Appl. Phys. Lett.* **2005**, *85*, 344.
- Van Weert, M.; Akopian, N.; Perinetti, U.; van Kouwen, M.; Algra, R.; Verheijen, M.; Bakkers, E.; Kouwenhoven, L. P.; Zwiller, V. *Nano Lett.* **2009**, *9*, 1989.
- Minot, E. D.; Kelkensberg, F.; van Kouwen, M.; van Dam, J. A.; Kouwenhoven, L. P.; Zwiller, V.; Borgström, M. T.; Wunnicke, O.; Verheijen, M. A.; Bakkers, E. P. A. M. *Nano Lett.* **2007**, *7*, 367.
- Singh, R.; Bester, G. *Phys. Rev. Lett.* **2009**, *103*, No. 063601.
- Heiss, D.; Jovanov, V.; Bichler, M.; Abstreiter, G.; Finley, J. J. *Phys. Rev. B* **2008**, *77*, 235442.
- Heiss, D.; Jovanov, V.; Caesar, M.; Bichler, M.; Abstreiter, G.; Finley, J. J. *Appl. Phys. Lett.* **2009**, *94*, No. 072108.
- Ramsay, A. J.; Boyle, S. J.; Kolodka, R. S.; Oliveira, J. B. B.; Skiba-Szymanska, J.; Liu, H. Y.; Hopkinson, M.; Fox, A. M.; Skolnick, M. S. *Phys. Rev. Lett.* **2008**, *100*, 197401.
- Press, D.; Ladd, T. D.; Zhang, B.; Yamamoto, Y. *Nature* **2008**, *456*, 218.
- Baier, M.; Findeis, F.; Zrenner, A.; Bichler, M.; Abstreiter, G. *Phys. Rev. B* **2001**, *64*, 195326.
- Spicer, W.; Lindau, I.; Skeath, P.; Su, C. Y.; Chye, P. *Phys. Rev. Lett.* **1980**, *44*, 420.
- Van Weert, M.; Wunnicke, O.; Roest, A.; Eijkemans, T.; Yu Silov, A.; Haverkort, J.; t Hooft, G.; Bakkers, E. *Appl. Phys. Lett.* **2006**, *88*, No. 043109.
- Chithrani, D.; Williams, R. L.; Lefebvre, J.; Poole, P. J.; Aers, G. C. *Appl. Phys. Lett.* **2004**, *84*, 978.
- Ediger, M.; Bester, G.; Badolato, A.; Petroff, P.; Karrai, K.; Zunger, A.; Warburton, R. *Nat. Phys.* **2007**, *3*, 774.
- Niquet, Y.-M.; Mojica, D. C. *Phys. Rev. B* **2008**, *77*, 115316.
- Empedocles, S. A.; Bawendi, M. G. *Science* **1997**, *278*, 2114.
- Warburton, R.; Urbaszek, B.; McGhee, E.; Schulhauser, C.; Hoge, A.; Karrai, K.; Gerardot, B.; Petroff, P. *Physica E* **2005**, *26*, 45.
- Reimer, M. E.; Dalacu, D.; Lapointe, J.; Poole, P. J.; Kim, D.; Aers, G. C.; McKinnon, W. R.; Williams, R. L. *Appl. Phys. Lett.* **2009**, *94*, No. 011108.
- Seidl, S.; Kroner, M.; Dalgarno, P. A.; Högele, A.; Smith, J. M.; Ediger, M.; Gerardot, B. D.; Garcia, J. M.; Petroff, P. M.; Karrai, K.; Warburton, R. J. *Phys. Rev. B* **2005**, *72*, 195339.
- Reimer, M. E.; Korkusinski, M.; Dalacu, D.; Levebvre, J.; Lapointe, J.; Poole, P. J.; Aers, G. C.; McKinnon, W. R.; Williams, R. L. *Phys. Rev. B* **2008**, *78*, 195301.
- Wagner, R.; Ellis, W. *Appl. Phys. Lett.* **1964**, *4*, 89.